A Transverse Bi-Rotor Aerial-Aquatic Robot Based on Coupled Vector Power System

Yi Sun, Youzhi Xu, Kaijie Lu, *Student Member, IEEE*, Pengfei Li, Huan Shen,
Jiajun Xu, *Member, IEEE*, Yadong Gao, Qijun Zhao, and Aihong Ji, *Member, IEEE*

***Abstract*—An aerial-aquatic robot integrates single-medium and cross-medium mobility capabilities, enabling the execution of sophisticated tasks in multimedium operational environments, such as ship hull inspection and cross-medium observations. Currently, improvements in underwater mobility capability are hindered due to the challenges introduced by the selection of power systems and control strategies, including the complexity of power systems and low integration of control systems. This article addresses the uncontrollable motion underwater of aerial-aquatic robots utilizing a transverse birotor platform for flight. A novel coupled vector power system concept is proposed and employed to develop an aerial-aquatic robot. This system incorporates a single vector underwater propeller, coupled with the existing vector birotor system of the flight platform, to achieve multimedium motion. The underwater linear motion capability is evaluated based on the test results of various combinations of the coupled vector power system. Furthermore, water-air multimedium motion experiments are conducted in an outdoor river to validate the superior motion control performance of the coupled configuration. These findings provide new insights for enhancing the multimedium motion capabilities of aerial-aquatic robots.**

***Index Terms*—Aerial-aquatic robot, coupled vector power system, multimedium motion, vector control strategy.**

I. Introduction

WITH the rapid advancement in drones and underwater vehicles, existing unmanned operation systems are capable of completing complex and diverse tasks in single-medium environments (air and water), such as wireless communications [1] and terrain mapping [2]. Despite their excellent capacities, drones or underwater vehicles often encounter challenges in detecting ship hulls above and below the waterline in multimedium environments. Moreover, using two separate sets of unmanned vehicles in each medium greatly complicates detection operations and reduces efficiency. Under this context, aerial-aquatic robots possessing single-medium and cross-medium motion capabilities have attracted widespread attention. Furthermore, aerial-aquatic robots should possess stable cross-medium mobility, along with exceptional capabilities in aerial flight and underwater motion [3].

In single-power systems, fixed-wing aerial-aquatic robots exhibit excellent aerodynamic efficiency and prolong endurance [4]. Despite these strengths, due to their dimensions, substantial thrust is required to overcome the drag caused by their wings during the transition from water to air [5], [6], [7], [8]. Furthermore, enhancing the active control of underwater motion in fixed-wing aerial-aquatic robots is necessary to improve overall multimedium mobility [9], [10].

On the other hand, multirotor aerial-aquatic robots are equipped with multiple rotors that generate considerable thrust to achieve smooth and swift departing from the water surface and perform flight motion. During cross-medium motion, disturbances induced by waves and water currents subtly impact the robot's performance [11], enabling vertical medium transition movements. Particularly for the miniaturized multirotor aerial-aquatic robots with blade diameters less than six inches [12], carrying a high-speed brushless motor to generate the required thrust presents challenges. The motors exhibit slow control effectiveness at slow speeds due to the resistance in the water medium. Conversely increasing motor speeds can lead to emergence from the water before the desired time [13], limiting its underwater motion capability. For these reasons, in addition to the water-air cross-medium process, research on multirotor aerial-aquatic robots focuses on the introduction of hybrid power systems [14], [15], [16], and methods such as vector control,

Received 11 December 2024; revised 24 March 2025; accepted 27 June 2025. Recommended by Technical Editor C. Shen and Senior Editor C Clevy. This work was supported in part by the National Natural Science Foundation of China under Grant 52075248 and Grant 52205018, in part by the Fundamental Research Funds for the Central Universities under Grant NP2024302, and in part by Postgraduate Research and Practice Innovation Program of Jiangsu Province under Grant KYCX25_0601. *(Corresponding author: Aihong Ji.)*

Yi Sun, Youzhi Xu, Huan Shen, and Jiajun Xu are with the Lab of Locomotion Bioinspiration and Intelligent Robots, College of Mechanical and Electrical Engineering, Nanjing University of Aeronautics and Astronautics, Nanjing 210016, China (e-mail: nuaa_sunyi@nuaa.edu.cn; xuyouzhi@nuaa.edu.cn; shenhuan99@nuaa.edu.cn; xujiajun@nuaa.edu.cn).

Kaijie Lu, Pengfei Li, Yadong Gao, and Qijun Zhao are with the College of Aerospace Engineering, Nanjing University of Aeronautics and Astronautics, Nanjing 210016, China (e-mail: lukaijie@nuaa.edu.cn; li_pengfei@nuaa.edu.cn; gydae@nuaa.edu.cn; zhaoqijun@nuaa.edu.cn).

Aihong Ji is with the Lab of Locomotion Bioinspiration and Intelligent Robots, College of Mechanical and Electrical Engineering, Nanjing University of Aeronautics and Astronautics, Nanjing 210016, China, also with the Jiangsu Key Laboratory of Bionic Materials and Equipment, Nanjing University of Aeronautics and Astronautics, Nanjing 210016, China, and also with the State Key Laboratory of Mechanics and Control for Aerospace Structures, Nanjing University of Aeronautics and Astronautics, Nanjing 210016, China (e-mail: meeahji@nuaa.edu.cn).

This article has supplementary material provided by the authors and color versions of one or more figures available at https://doi.org/10.1109/TMECH.2025.3584891.

Digital Object Identifier 10.1109/TMECH.2025.3584891

thereby improving the multimedium motion capability based on their outstanding cross-medium capabilities.

Drawing inspiration from the stable motion strategies of remotely operated vehicles (ROVs), the hybrid power system is designed with separate control systems for aerial flight and underwater motion, leveraging their respective capabilities tailored to specific single-medium environments [17]. With such merits, most hybrid power systems adopt a dual-layered separated design in terms of power layout [18], [19], [20], [21]. Despite the enhanced underwater motion capabilities of aerial-aquatic robots [22], [23], the dual-layered design of the hybrid power system increases the number of underwater actuators and lowers the integration of the control system.

Furthermore, modifying the initial underwater motion posture of the robot or incorporating vector control into the power system can effectively enhance the underwater motion capabilities of multirotor aerial-aquatic robots. For one thing, controlling the rotor's differential speed [24] or introducing a ballast system [25] switches the rotor's action surface from horizontal to vertical during underwater movement, to achieve a control logic for underwater mode consistent with that of aerial flight mode. For another, introducing vector control can improve the flexibility of its underwater motion. From the initial design of four vector rotors driven by single gear [26] to the configuration afforded by independent tilting mechanisms [27], rotors' vector control has been demonstrated to support the underwater motion of aerial-aquatic robots. Moreover, vector control can accommodate various power system configurations, such as X-type quadrotors, X8-type coaxial quadrotors [28], and trivector rotors [29].

However, in current research on aerial-aquatic robots, the issue of the center of gravity (C_G) across both water and air environments remains unclear. As the number of rotors decreases, the challenge of C_G configuration becomes more pronounced. In the X or X8 power systems configuration, the robot exhibits C_G is typically close to its action plane. This enables the generated thrust at a certain tilting angle approximately to act on C_G, realizing the desired effect of the thrust. In the case of the C_G designed at a specific distance from the action plane, the thrust generated by the vector rotor cannot directly translate into usable motion angles. Instead, it potentially introduces considerable moments that compromise the underwater stability of the robot. Therefore, the low C_G issue impacts their multimodal capabilities, rendering rotor vectorization methods unsuitable for direct application to all configurations of aerial-aquatic robots.

Currently, aerial-aquatic robots with a low C_G are primarily designed as birotor systems. However, most existing research employs a layered ROVs design to address the issue of uncontrollable underwater motion angles in vector tilt control [22], and no approach has yet achieved a high degree of integration between configuration and control, as shown in Fig. 1. Therefore, the coupled vector power system is introduced as a novel solution in the field of aerial-aquatic robots. This system effectively utilizes the inherent vector tilt structure and control mechanism of the transverse birotor design, addressing the problem while simultaneously enabling multimodal locomotion capabilities.

This article employs the transverse birotor platform as the flight platform, proposes a novel concept of a coupled vector power system, and develops an aerial-aquatic robot based on this innovative system. In addition, the vector control of the coupled vector power system is further optimized based on the control of transverse birotor configuration. By fully leveraging the vector tilting characteristics of the birotor system and introducing a single vector underwater propeller, it achieves a balanced state of forces and torques on the robot to effectively control its underwater motion posture. Moreover, the overall control integration of the robot is enhanced, enabling single-medium and multimedium motions. The comprehensive motion strategy of the aerial-aquatic robot based on the coupled vector power system is depicted in Fig.1.

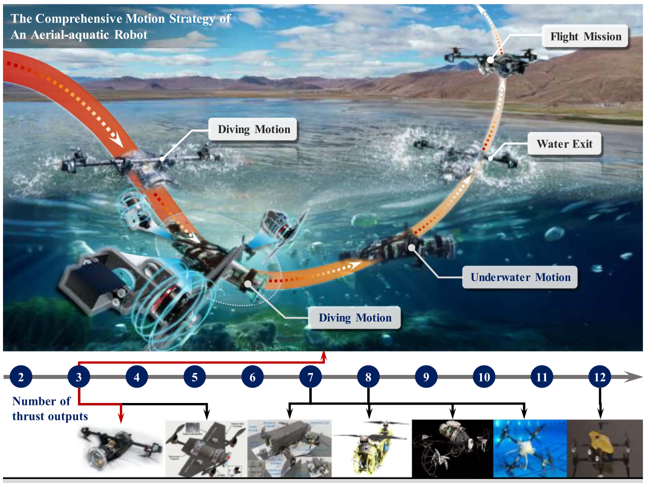

	Proposed	Zhejiang University[29]	NEZHA-mini[23]	Sun Yat-sen University[22]	BUAA [28]	Naviator [24]	NEZHA IV[14]
Low C_G	√	√	×	√	×	×	×
Rotors	2	3	4	2	8	8	4
Underwater propellers	1	0	3	5	0	0	8
Layered	×	×	√	√	×	×	√
Vectorized	√	√	×	√	√	×	×
Underwater stability	√	×	√	√	√	√	√

Fig. 1. Comprehensive motion strategy of the aerial-aquatic robot based on the coupled vector power system and comparison of motion performance.

The main contributions of this article are as follows.

1) It is clarified that rotor vectorization is not suitable for all aerial-aquatic robotic configurations. Furthermore, the importance of addressing the low C_G issue associated with rotor vectorization is emphasizes.
2) A new concept of a coupled vector power system is proposed, establishing a coupling relationship between a single vector underwater propeller and the vector birotor system. It offers a compact and highly integrated solution for the multimodal motion capabilities.
3) An aerial-aquatic robot based on the coupled vector power system is developed to address the issue of uncontrollable mobility angles when underwater using a low C_G configuration in vector control.

The rest of this article is organized as follows. Section II describes the overall structure and hardware system design of the robot. Section III presents the robot's kinematic and dynamic modeling. Section IV elaborates on the coupled vector power

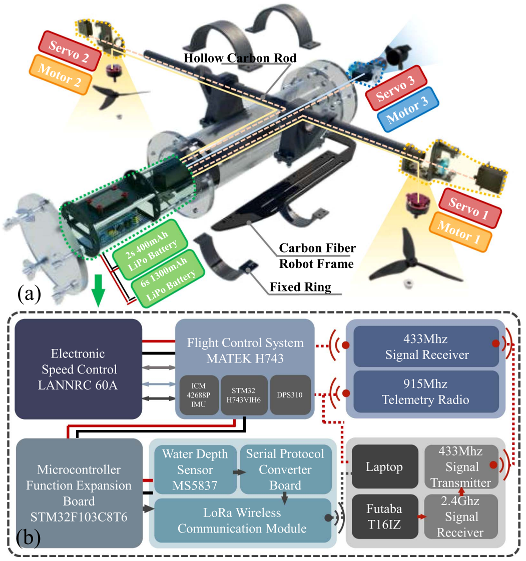

Fig. 2. (a) Overall configuration. (b) Electronic hardware diagram.

system's control performance and motion characteristics testing. Section V validates the designed robot's underwater linear motion and multimedium motion capabilities. Finally, Section VI concludes this article.

II. PROTOTYPE ROBOT DESIGN

A. Configuration

The robot has a cross-shaped configuration, with the fuselage arranged longitudinally with a waterproof sealed compartment, as shown in Fig. 2(a). Along the left and right sides of the main airframe, vector birotor power systems, with a wheelbase of 500 mm are mounted and expressed as l. A vector underwater propeller is installed at the rear structure, constituting an aerial-aquatic robot based on the coupled vector power system. The maximum dimensions of the robot are constrained within 574 mm × 422 mm × 180 mm (length × width × height), with a total mass of 1.8 kg.

For the buoyancy design of the robot, the buoyancy blocks of equal buoyancy size are placed at the rear of the robot. These blocks are made of rigid polyurethane foams, enabling the generation of slight positive buoyancy. Therefore, the center of buoyancy (C_B) is aligned slightly above the C_G. When the robot is floating on the water surface, it remains in a completely stationary state. By applying the 100 g counterweight, the robot can achieve approximate neutral buoyancy.

The vector tilting mechanism of the robot is crucial for the structure. The coupler in the vector tilting mechanism and the servo horn of the tilting servo motor are connected to a 15 mm hollow carbon rod, endowing the servo motor with a wide angular range of movement around the arm. The testing results demonstrate that the design can achieve a tilting range of 350° for vector rotors and 250° for the underwater propeller, greatly enhancing the flexibility of the power system and the controllability under manual operation.

The coupled vector power system consists of two T-MOTOR F60PROV 1750 kV brushless motors, a pair of GEMFAN 51466 V2 rotor blades, one 500 kV underwater brushless motor, a 60 mm diameter underwater propeller, and three GDW RS0708 270° servos. Given operations of the coupled vector power system in two different environments, waterproofing becomes markedly critical. For the brushless motors, only KAFUTER 704 sealant is applied at their wiring connections. Two waterproofing methods are employed for different internal components of the vector tilting servos. HOTOLUBE fully synthetic lubricating silicone grease is applied to the metal gear set at the top of the servo motor to prevent water ingress. Additionally, KAFUTER 704 sealant is deployed to seal the gap between the circuit control board at the bottom and outer shell of the servo motor, ensuring complete water prevention for the electronic circuitry system.

B. Avionics

In addition to the brushless motors and servos that come into direct contact with both media, all other electronic components and control boards are arranged inside the body. This is achieved through a transparent waterproof sealed compartment design, measuring 70 mm in diameter. Wiring from the rear of the body is sealed with epoxy resin. The electronic hardware framework is shown in the, as shown in Fig. 2(b). Due to the significant variation in power output among different components during operation, we have separated the voltage input sources for the robot. The GREPOW 6S 1300 mAh 75C and DUALSKY 2S 400 mAh 30C have been chosen to independently supply power to high-power components such as brushless motors and electronic speed controllers, as well as low-power components such as servos and control boards.

As the core of the control system, the flight controller board (MATEK H743 V3) is equipped with various sensors. It also receives signals from data transmission and the receiver, and outputs pulsewidth modulation (PWM) signals. Moreover, it is connected to the LR900M data transmission radio via serial port to adjust the robot's relevant motion parameters in real-time. For receiver selection, the Arkbird 433 MHz communication module is chosen to enhance communication capabilities across water surface. Additionally, in underwater mode, depth information of the robot's location often cannot be updated in real-time and displayed on the upper computer interface. Therefore, the STM32F103C8T6 system board is selected as the expansion board for the robot, which is connected to the MS5837 depth sensor and a depth information serial port board. It is combined with the WH-L1020-L-P LoRa wireless communication module to reduce the update delay time of depth information and allow for real-time display of depth information changes.

III. MODELING

A. Coordinate Definition

To study the six degrees of freedom motion of the aerial-aquatic robot, both ground coordinate system $\boldsymbol{R}_e : \{O_e, x_e, y_e, z_e\}$ and the body coordinate system $\boldsymbol{R}_b : \{O_b, x_b, y_b, z_b\}$ are introduced. The orientation of $\boldsymbol{R}_e$ follows

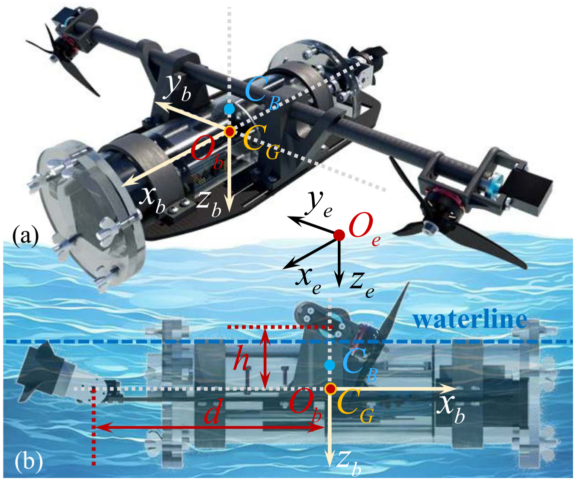

Fig. 3. Definition of coordinate system, C_G and C_B.

the "North-East-Down" convention, as illustrated in Fig. 3(a). The O_e is fixed at a point on the water-air interface. The gravitational acceleration $\mathrm{g} = 9.8\ \mathrm{m/s^2}$ aligns with the positive direction of the z_e. $\boldsymbol{R}_b$ is fixed to the robot, with its O_b coinciding with C_G. The x_b points towards the front of the robot, the z_b orients vertically downward and perpendicular to the plane of the body, and the y_b points to the right and parallel to the direction of the arms. $\boldsymbol{R}_b^e$ is defined as the rotation matrix that represents the transformation from $\boldsymbol{R}_b$ to $\boldsymbol{R}_e$, where $\mathrm{s}(\boldsymbol{\cdot})$, $c(\boldsymbol{\cdot})$and $\mathrm{t}(\boldsymbol{\cdot})$ correspond to $\sin(\boldsymbol{\cdot})$, $\cos(\boldsymbol{\cdot})$and $\tan(\boldsymbol{\cdot})$, respectively, as follows:

$$\boldsymbol{R}_b^e = \begin{bmatrix} c\theta c\psi & c\psi s\theta s\phi - s\psi c\phi & c\psi s\theta c\phi + s\psi s\phi \\ c\theta s\psi & s\psi s\theta s\phi + c\psi c\phi & s\psi s\theta c\phi - c\psi s\phi \\ -s\phi & s\phi c\theta & c\phi c\theta \end{bmatrix}. \quad (1)$$

B. Rigid Body Model of the Robot

1) Positive Buoyancy: To avoid the potential of the rotor's contact with water surface at high speeds during cross-medium motion, the robot is designed with slight positive buoyancy, mirrored by ρ_j, which represents the density of the operational medium. When $j = 1$, it refers to air, and the condition of $j = 2$ indicates water. C_G is located below the intersection of the vector birotor arm plane and the symmetrical plane of the arm and space at h from the center of the arm, to enhance flight stability. Additionally, C_G and the force application point of the tail rotor are collinear, with a spacing of d, to improve the underwater motion control of the robot. C_B is slightly higher than C_G, as shown in Fig. 3(b). The coordinate of C_B is denoted as $\boldsymbol{P}_B^b = [0 \quad 0 \quad -z_B]^T$. The restoring force$\boldsymbol{F}_{cb}^b$ and restoring moment $\boldsymbol{T}_{cb}^b$ generated by the robot can be represented as $-\boldsymbol{R}_b^{eT}(\boldsymbol{F}_G^e + \boldsymbol{F}_B^e)$ and $-\boldsymbol{P}_B^b \times \boldsymbol{R}_b^{eT}\boldsymbol{F}_B^e$.

2) Dynamics Model: In $\boldsymbol{R}_e$, the position vector $\boldsymbol{P}^e = [x \quad y \quad z]^T$ and attitude vector $\boldsymbol{\Theta}^e = [\phi \quad \theta \quad \psi]^T$ are defined, where φ, θ, and $\psi$are the roll, pitch, and yaw angles of the robot, respectively. In $\boldsymbol{R}_b$, the velocity vector $\boldsymbol{\nu}^b = [u \quad v \quad w]^T$ and the angular velocity vector $\boldsymbol{\omega}^b = [p \quad q \quad r]^T$ are determined. The robot is modeled as a symmetric rigid body for dynamics. The robot is influenced by a range of factors, including gravity F_G^e, buoyancy F_B^e, thrust $\sum_i \boldsymbol{F}_i^b$, and torque $\sum_i \boldsymbol{T}_{ci}^b$ from rotors and underwater propellers, added mass effects, fluid damping, as well as uncertain forces $\boldsymbol{F}_\Delta^e$ and torques $\boldsymbol{T}_\Delta^b$. i = 1, 2, 3 represent the motor serial numbers on the left side, right side, and tail of the robot, respectively. According to the Newton-Euler equations, the general form of the dynamic equations is described as (2) (3) shown at the bottom of the next page,where $\boldsymbol{M}_m$ and $\boldsymbol{J}_m$ represent the mass matrix and the rotational inertia matrix with respect to the coordinate axes. The robot is perfectly symmetric in the plane $x_b o_b z_b$, roughly symmetric in the plane $y_b o_b z_b$ and $x_b o_b y_b$, and O_b coincides with the C_G. The inertia matrix $\boldsymbol{M}_I$ can be represented as $\boldsymbol{M}_I = diag[\boldsymbol{M}_m, \boldsymbol{J}_m] = diag[m, m, m, I_{xx}, I_{yy}, I_{zz}]$. By ignoring the added mass effects caused by air on the robot, the added mass matrix $\boldsymbol{M}_a$ and the added inertia matrix $\boldsymbol{J}_a$ are denoted as $\boldsymbol{M}_a = diag[X_{\dot{u}}, Y_{\dot{v}}, Z_{\dot{w}}]$and $\boldsymbol{J}_a = diag[X_{\dot{p}}, Y_{\dot{q}}, Z_{\dot{r}}]$, respectively. Due to the presence of fluid viscosity, the drag coefficient and the drag torque coefficient are represented as $\boldsymbol{D}_M = diag[X_{u|u|}, Y_{v|v|}, Z_{w|w|}]$ and $\boldsymbol{D}_J = diag[X_{p|p|}, Y_{q|q|}, Z_{r|r|}]$.

Additionally, a coefficient k defines the robot's operating medium. In the water-entry state, with only a small portion of its top above water, the robot is considered fully submerged ($k = 1$). Since the rotor plane is above the water surface, the water-exit motion consists of the partial contact phase ($0<k<1$) and the full detachment phase ($k = 0$). Considering the effects of water viscosity and added mass, a multiphase flow model is established, with the simulation results shown in Fig. 4(a) and 4(b). Although the robot maintains control under disturbances, significant water surface depression and splashing induce periodic oscillations in yaw and pitch degrees of freedom. Therefore, the multimedium motion controller should be designed to ensure stable control across different motion modes and effectively mitigate disturbances.

C. Controller

The control algorithm of the robot is derived according to the Ardupilot firmware, and the controller framework is shown in Fig. 4(c). The position controller receives the desired position $\boldsymbol{P}_d$ from the multimedium motion controller and solves for the desired roll angle ϕ_d and pitch angle θ_d as inputs to the attitude controller. The attitude controller outputs the desired moments $\boldsymbol{T}_{da}$ and $\boldsymbol{T}_{du}$ in aerial and underwater modes based on the ϕ_d and θ_d from the position controller and the desired yaw angle ψ_d from the multimedium motion controller. Subsequently, these output angles are transmitted to the control allocator. Concurrently, the control allocator receives the desired forces F_{daz} and $\boldsymbol{F}_{du}$from the position controller, thus allocating the desired rotational speeds n_{di}, and desired tilt angles $\alpha_{di}$and β_d to the coupled vector power system, enabling precise control of motor and servo outputs. Finally, the robot utilizes sensors embedded in the main control module to obtain $\boldsymbol{\Theta}^e$, $\boldsymbol{\omega}^b$, $\boldsymbol{P}^e$, and $\boldsymbol{\nu}^b$, which are transmitted to the attitude controller and position controller to complete the control loop.

Given the necessary capacities to transit seamlessly between two media and maintain underwater maneuverability, the control allocation is critical in controller framework, due to its direct impact on the coupled vector power system. We define the tilt angle of the rotor as α_i and the tilt angle of the underwater propeller as β. h is the distance from C_G to the center of the robotic arm, and d is the distance from C_G to the thrust application point of the underwater propeller. Moreover, the initial position of the tilt angle is determined as 0° along the positive x_b, as marked by the dashed lines in Fig. 4(c).

In the aerial mode, the tail underwater propeller remains fixed and stationary, and the vector rotors on both sides generate thrust and torque. In the water-exit motion, the rotor plane remains consistently above the water surface to ensure efficiency and stability. Accordingly, the control allocation for thrust and torque in aerial flight and water-exit motion is consistent, as shown in (4). Here, F_{az},T_{ax},T_{ay}, and T_{az} represent the lift and the control moments around *x*, *y*, and *z* axes, respectively, as follows:

$$\begin{bmatrix} -1 & 0 & -1 & 0 \\ l/2 & 0 & -l/2 & 0 \\ 0 & -h & 0 & -h \\ 0 & l/2 & 0 & -l/2 \end{bmatrix} \begin{bmatrix} F_1 \cdot \sin\alpha_1 \\ F_1 \cdot \cos\alpha_1 \\ F_2 \cdot \sin\alpha_2 \\ F_2 \cdot \cos\alpha_2 \end{bmatrix} = \begin{bmatrix} F_{az} \\ T_{ax} \\ T_{ay} \\ T_{az} \end{bmatrix}. \tag{4}$$

In underwater motion, the vector rotors and underwater propeller work together to create a coupled vector power system, producing forces and moments $\boldsymbol{\tau}_u = [\boldsymbol{F}_u \quad \boldsymbol{T}_u]^T$.$\boldsymbol{F}_u$ and $\boldsymbol{T}_u$ are composed of force components F_{ux}, F_{uy}, and F_{uz} in *x*-, *y*-, and *z*-directions, as well as the moment components T_{ux},T_{uy}, and T_{uz}. The control variables for rotors and an underwater propeller constitute generated thrust, expressed as $\boldsymbol{F} = [F_1 \quad F_2 \quad F_3]^T$. The tilt angles α_1, α_2, and β are constant. The system outputs of forces and moments are as follows:

$$\boldsymbol{\tau}_u = \begin{bmatrix} F_{ux} \\ F_{uy} \\ F_{uz} \\ T_{ux} \\ T_{uy} \\ T_{uz} \end{bmatrix} = \begin{bmatrix} \cos\alpha_1 & \cos\alpha_2 & \cos\beta \\ 0 & 0 & 0 \\ \sin\alpha_1 & \sin\alpha_2 & \sin\beta \\ \frac{l}{2}\sin\alpha_1 & -\frac{l}{2}\sin\alpha_2 & 0 \\ -h\cos\alpha_1 & -h\cos\alpha_2 & d\sin\beta \\ \frac{l}{2}\cos\alpha_1 & -\frac{l}{2}\cos\alpha_2 & 0 \end{bmatrix} \begin{bmatrix} F_1 \\ F_2 \\ F_3 \end{bmatrix} = \boldsymbol{B}_2 \boldsymbol{F} \tag{5}$$

where $\boldsymbol{B}_2$ is the thrust allocation matrix, determined by the arrangement of the coupled vector power system. To allocate the desired output forces and moments $\boldsymbol{\tau}_{du} = [\boldsymbol{F}_{du} \quad \boldsymbol{T}_{du}]^T$ to each actuator, the generalized inverse matrix method is introduced and expressed as

$$\boldsymbol{F}_d = \boldsymbol{B}_2^{+} \boldsymbol{\tau}_{du} \tag{6}$$

where $\boldsymbol{B}_2^{+}$ is the generalized inverse control distribution matrix. This result allows for determining the final thrust magnitude of the coupled vector power system during underwater motion.

IV. COUPLED VECTOR POWER SYSTEM

A. Consideration of Power System

Vectorizing the multirotor power system to effectively operate both media is an innovative solution. Notably, underwater motion cannot be achieved solely with two sets of vector rotors for a robot equipped with vector birotors as a flight platform. This is attributed to the specific distance between the robot's C_G and the force application plane of the rotors, which provides the necessary control torque for aerial mode. Nevertheless, the torque generated by this low C_G design prevents the robot from exclusive reliance on a single vector birotor power system to achieve fixed-angle motion underwater. Specifically, when the two rotors tilt and rotate underwater, the low C_G configuration creates substantial moments T_1 and T_2 about C_G, as shown in Fig. 4(d).

To avoid the introduction of excessive underwater thrusters for underwater motion control, we incorporate only one single vector underwater propeller at the rear of the robot, generating T_3 in the opposite direction. With this incorporation, a coupled relationship with the vector birotors is developed, thereby addressing the critical issue of force and torque imbalance during underwater motion. The overall force and torque are illustrated in Fig. 4(d), with the expression as (7) shown at the bottom of the next page. F_x, F_y, F_z, T_x, T_y, and $T_z$represent the forces and moments acting on the robot in the *x*-, *y*-, and *z*-directions during the underwater motion state.

During fixed-angle motion, the angular accelerations around the *x*, *y*, and *z* axes should all be zero. Along the *x*-axis, the motion should be uniform or uniformly accelerated, while the acceleration along the *z*-axis should remain as constant as possible during fixed-angle motion to minimize the impact of angular acceleration, thereby ensuring force and moment balance. It should be noted that we coordinate the thrust magnitude and tilt angle of the vector rotors on both sides when submerged to avoid the generation of additional torque that potentially affects the target angle motion. During operation, the underwater propeller generates a counter torque around z_b.This effect is disregarded as the underwater propeller can generate the required thrust for the system at low rotational speeds, resulting in minimal torque influence. Although employing rotors presents a potential

---

$$\begin{aligned} &\boldsymbol{R}_b^e \sum_i \boldsymbol{F}_i^b - \boldsymbol{R}_b^{eT}(\boldsymbol{F}_G^e + \boldsymbol{F}_B^e) + (\boldsymbol{M}_m - k\boldsymbol{M}_a)\dot{\boldsymbol{\nu}}^b \\ &\quad - \left[(\boldsymbol{M}_m - k\boldsymbol{M}_a)\boldsymbol{\nu}^b\right] \times \boldsymbol{\omega}^b - k\boldsymbol{D}_M \boldsymbol{\nu}^b \left|\boldsymbol{\nu}^b\right| + \boldsymbol{F}_\Delta^e = m \cdot \dot{\boldsymbol{\nu}}^b \end{aligned} \tag{2}$$

$$\begin{aligned} &\sum_i \boldsymbol{T}_i^b + \sum_i \boldsymbol{T}_{ci}^b - \boldsymbol{P}_B^b \times \boldsymbol{R}_b^{eT} \boldsymbol{F}_B^e + (\boldsymbol{J}_m - k\boldsymbol{J}_a)\dot{\boldsymbol{\omega}}^b + (k\boldsymbol{M}_a \boldsymbol{\nu}^b) \times \boldsymbol{\nu}^b \\ &\quad - \left[(\boldsymbol{J}_m - k\boldsymbol{J}_a)\boldsymbol{\omega}^b\right] \times \boldsymbol{\omega}^b - k\boldsymbol{D}_J \boldsymbol{\omega}^b \left|\boldsymbol{\omega}^b\right| + \boldsymbol{T}_\Delta^b = \boldsymbol{J}^b \dot{\boldsymbol{\omega}}^b + \boldsymbol{\omega}^b \times (\boldsymbol{J}^b \boldsymbol{\omega}^b) \end{aligned} \tag{3}$$

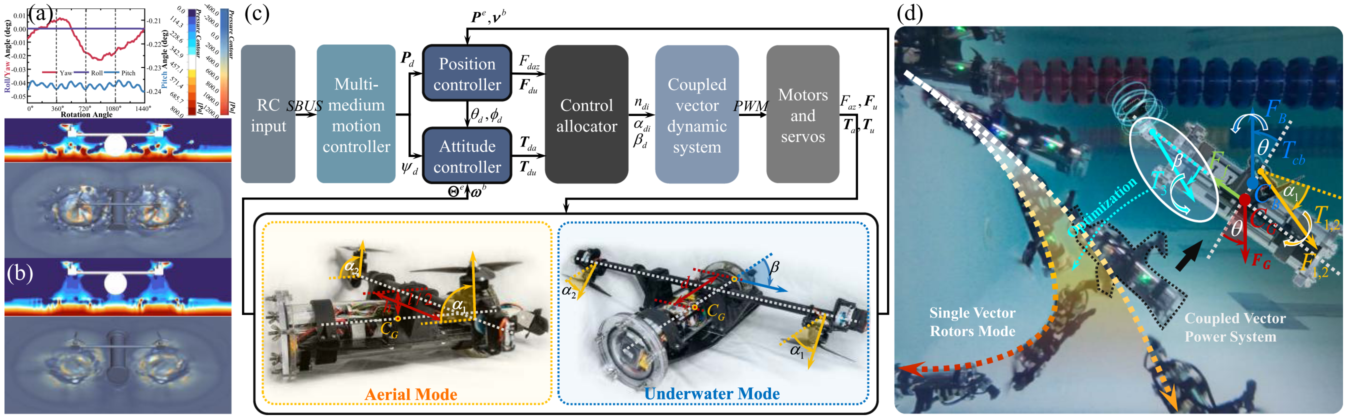

Fig. 4. (a) Partial contact phase(0<k<1). (b) Full detachment phase (k = 0). (c) Controller framework. (d) Analysis with and without coupled vector power system.

alternative to balance the small torque generated by the underwater propeller, it increases the instability of the robot during fixed-angle motion. On this basis, the solution of (7) can be further simplified as $T_y = 0$, resulting in the relationship among θ, F_1, F_2, and F_3

$$\sin\theta = \frac{2hF_1\cos\alpha_1 - dF_3\sin\beta}{z_B F_B}. \tag{8}$$

For the desired motion angle, F_1 and F_3 are obtained from different throttle values and thrust combinations tested in Section IV-B. F_1 is determined to ensure that the rotor maintains efficient force output within a reasonable range. Furthermore, α_1 is determined based on the motion angle to derive the relationship between F_3 and β.

B. Single Vector Power System

The coupling point ensures that the vector rotors output control force and torque consistently in water and air. Through performance testing of the rotor and underwater propeller in different mediums, the variation patterns of different throttle and thrust output value are obtained, establishing a mutual mapping relationship between throttle output values, PWM signal values, and thrust output values to enhance the stability of vector rotors during continuous underwater operation.

However, due to water resistance, rotor blades rotating underwater fail to exhibit the high rotational speed characteristics consistent with the motion in the air [6], [25], and are susceptible to problems such as reduced power efficiency and overload. For this consideration, testing the force and power of a single rotor and underwater propeller in different media necessitated to verify the realizability of the coupled vector power system. The underwater motion control by a separate vector birotor power system also needs testing to illustrate the necessity of a coupled vector power system.

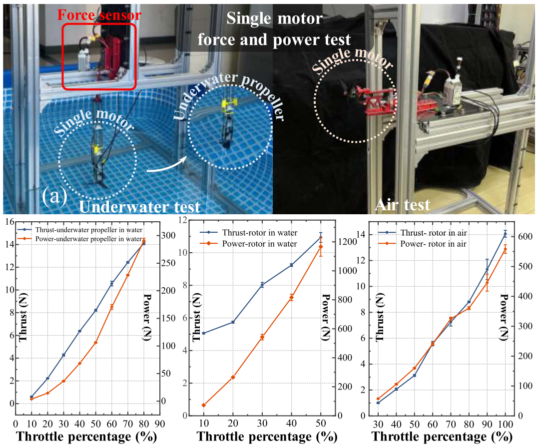

Fig. 5. Force and power tests of a single rotor and underwater propeller.

The system test platform is presented in Fig. 5. Specifically, the force sensor allows for the real-time monitoring of power system's current, voltage, and power generated, and its axial direction coincides with that of the thrust generated by the power system.

The results for the rotor in air and underwater propeller in water exhibit a roughly linear growth in the corresponding medium. Moreover, the underwater propeller can produce stable thrust at low power, and the rotor generates high thrust at fast speed.

$$\begin{cases} F_x = (F_G - F_B)\cdot\sin\theta + F_1\cdot\cos\alpha_1 + F_2\cdot\cos\alpha_2 + F_3\cdot\cos\beta - F \\ F_y = 0 \\ F_z = (F_G - F_B)\cdot\cos\theta + F_1\cdot\sin\alpha_1 + F_2\cdot\sin\alpha_2 + F_3\cdot\sin\beta \\ T_x = \frac{l}{2}(F_1\cdot\sin\alpha_1 - F_2\cdot\sin\alpha_2) + T_{c3} \\ T_y = -h(F_1\cdot\cos\alpha_1 + F_2\cdot\cos\alpha_2) + F_3\cdot\sin\beta\cdot d + z_B F_B\sin\theta \\ T_z = \frac{l}{2}(F_1\cdot\sin\alpha_1 - F_2\cdot\sin\alpha_2). \end{cases} \tag{7}$$

Regarding the rotor performance underwater, the growth rate of the generated thrust is lower than that of power with the increasing percentage of throttle in steps. When the percentage rises to approximately 50%, the rotor generates more power and produces a current approaching the maximum continuous current imposed by the ESC. In the case of 10% operating throttle at a reduced rotational speed, the average thrust and power generated are 5.06 N and 73.2 W, respectively. This outcome verifies the feasibility of the five-inch rotor in underwater motion. Therefore, in order to avoid the phenomena such as low force efficiency due to the excessive power generated by the rotor rotating underwater, the maximum output range of the rotor underwater is controlled within 20% throttle primarily around 10% throttle.

Finally, we tested the motion of the separate vector birotors in pools at different depths. At 40 cm water depth, the robot quickly contacts the bottom in only about 1 s, and the pitch angle gradually increases during motion. In addition, the robot develops attitude inversion in the low C_G configuration within 2 s in a pool at 1.2 m depth, as shown in Fig. 4(d). The existence of T_1 and T_2 will increase the pitch angle to 90° in a fairly short period, suppressing subsequent underwater motion of the robot. For this reason, the balance of the total moment of the fuselage around the Y-axis, i.e., the pitch moment, is critical during the fixed-angle motion underwater.

C. Coupled Vector Power System

For a robot floating on the water surface, the key to accomplishing further underwater motion lies in stable and controllable fixed-angle motion. Based on the equilibrium analysis of forces and moments in Section IV-A and the test results of different power systems in Section IV-B, the fixed-angle motion underwater is evaluated in a swimming pool with a depth range of 0.7–1.2 m to validate the effect of the coupled vector power system. The maximum motion time for the robot to dive from the water surface to the bottom is about 2.8 s constrained by the experimental depth range. Despite such limitation, this test environment allows for evaluating the effectiveness of the robot's control of a fixed angle. We analyze the attitude change information of pitch angle, acceleration along z_b(Acc-z_b), and angular rate around y_b(Angular rate-y_b) of the robot using the IMU and log storage module of flight control board. The fixed-angle motion underwater is categorized into small-angle (0–30°) and large-angle (45–60°) motion and is tested experimentally, as illustrated in Fig. 6(a).

In the experiment of small-angle motion, nine groups of data are obtained, and the average sailing angles are $-2.7°$, $-6.39°$, $-9.36°$, $-11.76°$, $-14.46°$, $-16.63°$, $-19.82°$, $-23.21°$, and $-26.25°$. The angle alternations can be controlled at about three degrees, realizing the fine control of small-angle motion. Small-angle motions enable the robot to maintain fixed-angle motions for 1.1–2.8 s, which is 39–100% of the motion time. From the analysis in Fig. 6(b), the robot undergoes a sudden change in the angular rate from positive to negative upon receiving the command. This is attributed to the tip portion of the rotor is exposed to the water surface in the tilting attitude, which prevents the thrust from reaching its maximum value and makes the robot unstable upon moving. Furthermore, at the starting moment, the underwater propeller responds faster than the rotor to generate thrust responsible for stabilization. When the robot is completely submerged, attaining the established small-angle motion state needs a specific time interval. With the balanced control of the forces and moments, the Angular rate-y_b applied to the robot can be stabilized at approximately 0 °/s.

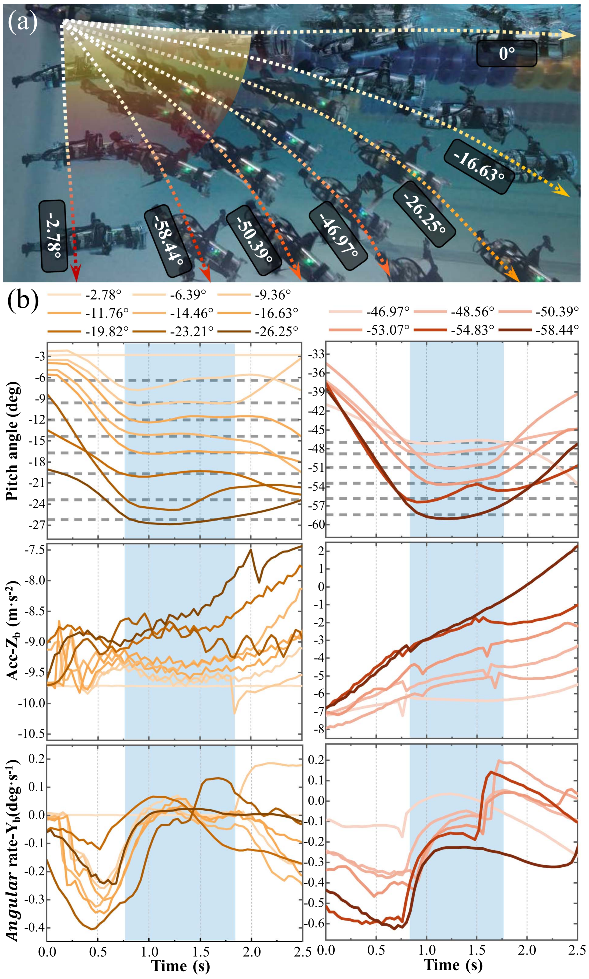

Fig. 6. (a) Fixed-angle motion underwater includes small-angle and large-angle motions. (b) Experimental testing of underwater fixed-angle motion under the coupled vector power system.

For the large-angle motion underwater experiment, six groups of underwater sailing motions with different fixed angles are investigated, and the average sailing angles include $-46.97°$, $-48.5°$, $-50.39°$, $-53.07°$, $-54.83°$, and $-58.44°$. As a result, a certain gradient change in the motion angle can be attained in the large-angle motion. However, the tilting angle of the vector birotors in the large-angle motion is increased to achieve the established motion angle. Furthermore, the force arm generated by the rotors is shortened, increasing the rotor rotational speed for improved thrust. Such improvement promotes the achievement of the balanced control of the forces and moments exerted on the robot. However, increasing the thrust generated by the rotor underwater is not ideal. The accuracy of the coupled vector

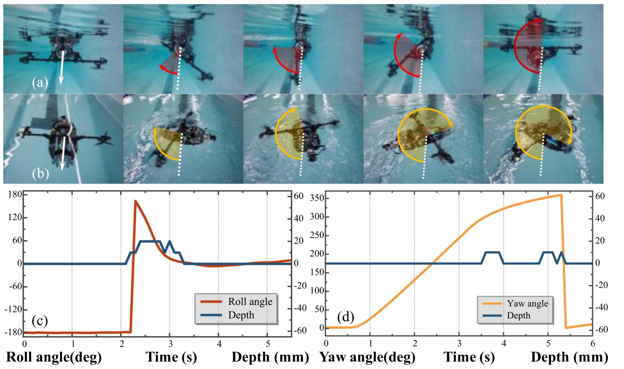

Fig. 7. (a) and (c) Attitude correction motion. (b) and (d) 360° planar rotation.

power system's control of the Angular rate-y_b is greatly reduced due to the shortening of the force arm and the accompanying increase in generated power.

As a result, fifteen sets of motion data for fixed-angle sailing are acquired for the experiment, on water entry angles ranging from 0–60°. Among them, stable underwater motion is achieved primarily in the pitch angle range between 0 and -30°, and the most stable motion occurs with an approximately horizontal attitude. Although the motion control accuracy of the coupled vector power system on the robot gradually decreases with the increasing motion angle, the robot does not roll and flip over in the experimental test.

In addition to the fixed-angle motion control of the coupled vector power system, the robot is designed to be slightly positively buoyant, with C_B adjusted to a close proximity to C_G. However, when a robot collides with an unknown obstacle underwater, the body may flip over due to the attitude deviation. The inverted attitude state can be corrected with the vector tilting capability of the coupled vector power system. The attitude correction motion of the robot is demonstrated in Fig. 7(a) and (c). Furthermore, with the yaw moment of the vector dual rotor, the robot can realize its 360° planar rotation on the water surface, as shown in Fig. 7(b) and (d). After continuous rotation tests, the center of rotation did not deviate substantially from the initial position. The active correction motion and planar rotation motion further enhance the abilities to move and adjust on the water surface.

V. EXPERIMENTS

A. Motion Patterns and Strategies

The robot's motion modes include aerial flight, surface floating, vertical dive, underwater fixed-angle motion, active uplift, cross-medium motion, planar rotation, and attitude correction, among others. Among these, vertical dive, small-angle motion, and active uplift are represented by downward, diagonally downward to the right, and upward arrow symbols, respectively, as shown in Fig. 8. These various motion modes can not only be partially combined to enhance underwater motion capabilities, as shown in Fig. 8, but also combined to form a comprehensive air-water-air multimodal motion strategy, as shown in Figs. 1 and 9.

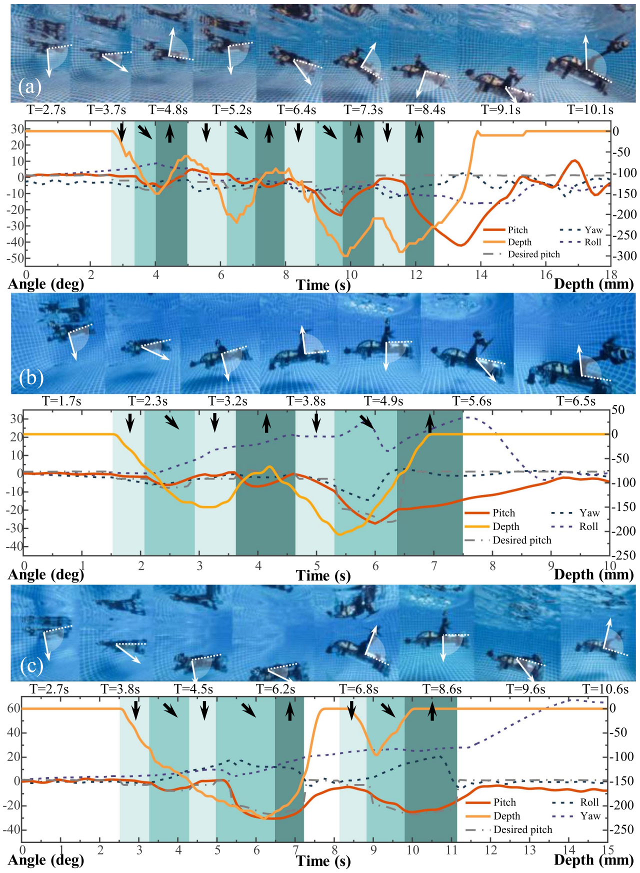

Fig. 8. Experimental test of underwater linear motion. (a) and (b) Continuous stepwise motions. (c) Interrupted stepwise motions.

During aerial and emergence motion, the servo tilt angles on both sides and the thrust output from the brushless motors work in coordination to enable motion across six degrees of freedom. In underwater motion, the coupled output of the vector rotor and vector underwater propeller enables linear underwater motion. Based on the analysis in Section IV, the most stable vertical dive state is considered the initial state for underwater motion. Once the robot reaches a position below the water surface, a stepwise underwater motion is initiated. The stepwise motion ensures continuous vector tilt angles, thereby guaranteeing controllable motion angles and is defined as the formation of continuous and controllable underwater motion capabilities through any combination of the robot's underwater motion modes.

B. Underwater Linear Motion

Despite the ability to enter underwater smoothly with a horizontal attitude, the robot exhibits various motion stability degrees across different combinations in stepwise motion, justifying the need to reasonably arrange the motion states operated by the coupled vector system.

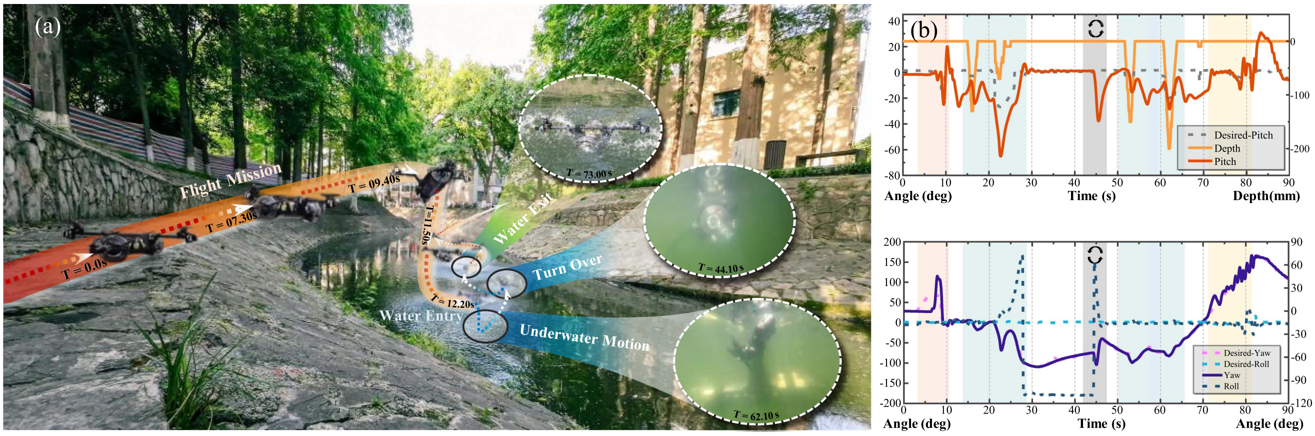

Fig. 9. (a) Outdoor testing for multimedium motions, including aerial flight, underwater mobility, surface movement, attitude correction, and cross-medium motion. (b) Experimental results of depth and attitude of the multimedium motions.

First, the underwater linear motion is achieved by the "vertical dive-small angle motion-active uplift" configuration. Specifically, three executions of this configuration enable approximately a 200 cm range of the linear motion within 11 s. From Fig. 8(a), it can be found that the change in the pitch angle of the robot is consistent with that of the diving depth, and the fluctuation range of the roll angle and the yaw angle is small. Moreover, the actual linear trajectory coincides with the desired one, indicating a better capability of underwater linear motion.

Second, based on the combination of "vertical dive-small angle motion-active uplift", the second combination can be designed by employing the vertical dive movement state as the connection point, i.e., "vertical dive-small angle motion-vertical dive-active uplift". We superimpose these two combinations to form the stepwise motion, as shown in Fig. 8(b). During another switch from small-angle motion to vertical downward motion, its roll degree of freedom oscillates. The main reason is that both birotors continue to output forces and moments during the robot's tilting, aggravating the roll fluctuation in small-angle motion. Furthermore, due to the pitch angle at a certain angle to the horizontal attitude during active uplift, this pitch angle cannot reach the horizontal attitude of the first two dive movements during the third consecutive vertical dive motion, further affecting the roll and yaw angles. Consequently, the actual trajectory displays an angular error of about 10° drifting from the linear desired trajectory.

Similarly, the motion strategy involving the vertical dive motion state as the connection point is adopted, constituting the third combination of "vertical dive-small angle motion-vertical dive-small angle motion-active uplift". The need to avoid the fluctuation of pitch angle during the transition from active uplift to vertical dive and reduce the roll angle oscillation arising from the motion state is considered. To fulfill these purposes, the active uplift motion is extended until the robot's emergence above the water surface, as shown in Fig. 8(c). Compared to the second combination, the robot exhibits improved control of roll degrees of freedom in two consecutive vertical dives. Moreover, the two consecutive small-angle motions rapidly increase the underwater motion depth, demonstrating better control of the coupled vector power system for the pitch angle in a limited depth of 40 cm. In addition, the robot surfaces and enters an unpowered floating state, and the yaw direction is disturbed due to the roll fluctuation in the active uplift motion and the pool water flow. The resulting linear trajectory exhibits an approximately 20° angle with the desired linear trajectory. Finally, the floating robot can utilize other combinations for further underwater linear motion after performing the third combination.

C. Multimedium Motion

An outdoor river is selected to test the cross-medium and single-medium motion performance. Specifically, aerial flight (denoted by orange shading), underwater and surface motion (green shading), attitude correction (gray shading), and cross-medium motions (yellow shading) are explored experimentally, as shown in Fig. 9.

First, the robot takes off from the shore and lands on the water surface, realizing the air-to-water conversion. Second, the robot enters the water at 15.5 s and performs a set of "vertical dive-active uplift" motions. Due to the oscillating water surface after the robot's landing, the initial attitude during the vertical dive motion is not completely horizontal, instead, it is in a fluctuating state. Despite such an influence, the active uplift motion can quickly restore the smooth attitude of the robot, as shown in Fig. 9. At 19.8 s, during the first continuous stepwise movement of "vertical dive-small angle motion-active uplift," the robot is interfered by unknown obstacles during the fixed-angle motion. This interference arises from the presence of many obstacles and the undetectable environment underwater. As a result, an abrupt variation occurs in the rate of change in pitch angle, followed by a 180-degree flip-over in the direction of roll, and the robot emerges above the surface at 28.88 s. With the coupled vector power system, the robot can achieve attitude correction and recover to a floating state on the water surface at 47.1 s. After resuming the floating state, it repeats the combined motion of "vertical dive - active uplift," performs a short-distance straight-line motion on the water surface, and connects again to the continuous stepped motion of "vertical dive - fixed-angle motion - active uplift."

Finally, under the output control of the vector birotors, the robot performs the water-to-air conversion motion at 73 s, with complete detachment and subsequent flight at 79.1 s. During the water exit process, consistent with the simulation results, as shown in Fig. 4(a), oscillations occur in the pitch and yaw degrees of freedom. However, the robot effectively handles disturbances during the transition. After detaching from the water surface, the robot is able to maintain favorable attitude control and successfully transition to free-flight motion.

VI. CONCLUSION

In this article, the importance of addressing low C_G issue associated with rotor vectorization is emphasized. Additionally, a novel concept of coupled vector power system is proposed and employed to develop an aerial-aquatic robot. The system introduces only a single vector underwater propeller at the rear of the vector birotors' flight platform, and couples it with the vector birotors for output control. To reduce the power system's complexity and improve the control integration of the robot, the coupled vector power system takes full advantage of the vector control available in the flight platforms and integrates the motion performances of the two different power systems in respective medium. This presents an effective solution to the problems of force and moment imbalance in underwater motion of aerial-aquatic robots with transverse dual rotors in low C_G configurations. Based on considerable experimental tests in indoor pool and outdoor river scenarios, the aerial-aquatic robot built upon the proposed concept has the ability to operate stably along the target angle, with the controllable angle covering the range of 0–60°, and to realize the fine control of the angle of about three degrees. Moreover, through the combination of arbitrary motion states operated by the coupled vector power system, the robot can perform three combinations of stepwise underwater linear motions. Finally, the aerial-aquatic robot based on the coupled vector power system implements single-medium and cross-medium motions within an outdoor river, verifying the reasonableness and feasibility of the overall design, power system, and control scheme of the system.

In follow-up research, influencing factors (water current disturbance and water depth variation) and more robust adaptive controllers should be introduced to optimize the coupled vector power system, thereby achieving more accurately and flexibly control over the underwater motion. Moreover, the coupled vector power system has great potential in the medium conversion, opening a new avenue for cross-medium motions.

REFERENCES

[1] Y. Zeng, R. Zhang, and T. J. Lim, "Wireless communications with unmanned aerial vehicles: Opportunities and challenges," *IEEE Commun Mag.*, vol. 54, no. 5, pp. 36–42, May 2016, doi: 10.1109/MCOM.2016.7470933.

[2] H. Zhou, H. Kong, L. Wei, D. Creighton, and S. Nahavandi, "Efficient road detection and tracking for unmanned aerial vehicle," *IEEE Trans. Intell. Transp. Syst.*, vol. 16, no. 1, pp. 297–309, Feb. 2015, doi: 10.1109/TITS.2014.2331353.

[3] Y. Sun et al., "Design and theoretical research on aerial-aquatic vehicles: A review," *J. Bionic Eng.*, vol. 20, no. 6, pp. 2512–2541, 2023, doi: 10.1007/s42235-023-00418-x.

[4] Z. Wei, Y. Teng, X. Meng, B. Yao, and L. Lian, "Lifting-principle-based design and implementation of fixed-wing unmanned aerial–underwater vehicle," *J. Field Robot.*, vol. 39, no. 6, pp. 694–711, 2022, doi: 10.1002/rob.22071.

[5] W. Weisler, W. Stewart, M. B. Anderson, K. J. Peters, A. Gopalarathnam, and M. Bryant, "Testing and characterization of a fixed wing cross-domain unmanned vehicle operating in aerial and underwater environments," *IEEE J. Ocean. Eng.*, vol. 43, no. 4, pp. 969–982, Oct. 2018, doi: 10.1109/JOE.2017.2742798.

[6] X. Sun, J. Cao, Y. Li, and B. Wang, "Design and field test of a foldable wing unmanned aerial–underwater vehicle," *J. Field Robot.*, vol. 41, no. 2, pp. 347–373, 2024, doi: 10.1002/rob.22265.

[7] W. Stewart, W. Weisler, M. Anderson, M. Bryant, and K. Peters, "Dynamic modeling of passively draining structures for aerial–Aquatic unmanned vehicles," *IEEE J. Ocean. Eng.*, vol. 45, no. 3, pp. 840–850, Jul. 2020, doi: 10.1109/JOE.2019.2898069.

[8] F. Rockenbauer et al., "Dipper: A dynamically transitioning aerial-aquatic unmanned vehicle," in *Proc. Conf. Robot., Sci. Syst.*, 2021, pp. 1–9.

[9] W. Stewart et al., "Design and demonstration of a seabird-inspired fixed-wing hybrid UAV-UUV system," *Bioinspiration Biomimetics*, vol. 13, no. 5, 2018, Art. no. 056013, doi: 10.1088/1748-3190/aad48b.

[10] R. Siddall, A. Ortega Ancel, and M. Kovač, "Wind and water tunnel testing of a morphing aquatic micro air vehicle," *Interface Focus*, vol. 7, no. 1, 2017, Art. no. 20160085, doi: 10.1098/rsfs.2016.0085.

[11] Y. Jin, Y. Bi, C. Lyu, Y. Bai, Z. Zeng, and L. Lian, "Nezha-IV: A hybrid aerial underwater vehicle in real ocean environments," *J. Field Robot.*, vol. 41, no. 2, pp. 420–442, 2024, doi: 10.1002/rob.22274.

[12] L. Li et al., "Aerial-aquatic robots capable of crossing the air-water boundary and hitchhiking on surfaces," *Sci. Robot.*, vol. 7, 2022, Art. no. eabm6695, doi: 10.1126/scirobotics.abm6695.

[13] J. Zha, E. Thacher, J. Kroeger, S. A. Mäkiharju, and M. W. Mueller, "Towards breaching a still water surface with a miniature unmanned aerial underwater vehicle," in *Proc. Int. Conf. Unmanned Aircr. Syst.*, 2019, pp. 1178–1185.

[14] C. Lyu et al., "Toward a gliding hybrid aerial underwater vehicle: Design, fabrication, and experiments," *J. Field Robot.*, vol. 39, no. 5, pp. 543–556, 2022, doi: 10.1002/rob.22063.

[15] D. Lu et al., "Design, fabrication, and characterization of a multimodal hybrid aerial underwater vehicle," *Ocean Eng.*, vol. 219, 2021, Art. no. 108324, doi: 10.1016/j.oceaneng.2020.108324.

[16] R. Hu et al., "Modeling, characterization and control of a piston-driven buoyancy system for a hybrid aerial underwater vehicle," *Appl. Ocean Res.*, vol. 120, 2022, Art. no. 102925, doi: 10.1016/j.apor.2021.102925.

[17] G. Chen, A. Liu, J. Hu, J. Feng, and Z. Ma, "Attitude and altitude control of unmanned aerial-underwater vehicle based on incremental nonlinear dynamic inversion," *IEEE Access*, vol. 8, pp. 156129–156138, 2020, doi: 10.1109/ACCESS.2020.3015857.

[18] R. T. S. d. Rosa et al., "A comparative study on sigma-point Kalman filters for trajectory estimation of hybrid aerial-aquatic vehicles," in *Proc. IEEE/RSJ Int. Conf. Intell. Robots Syst.*, 2018, pp. 7460–7465.

[19] Y. Gao, H. Zhang, H. Yang, S. Tan, T. A. Gulliver, and T. Lu, "Trans-domain amphibious unmanned platform based on coaxial counter-propellers: Design and experimental validation," *IEEE Access*, vol. 9, pp. 149433–149446, 2021, doi: 10.1109/ACCESS.2021.3125138.

[20] Y. Gao, H. Zhang, G. Li, M. Zhou, H. Yin, and T. A. Gulliver, "Analysis of trans-domain motion process of bullet-shaped trans-domain amphibious vehicle," *J. Field Robot.*, vol. 41, no. 1, pp. 68–92, 2024, doi: 10.1002/rob.22244.

[21] P. L. J. Drews, A. A. Neto, and M. F. M. Campos, "Hybrid unmanned aerial underwater vehicle: Modeling and simulation," in *Proc. IEEE/RSJ Int. Conf. Intell. Robots Syst.*, 2014, pp. 4637–4642.

[22] S. Wu et al., "Design and demonstration of a tandem dual-rotor aerial–Aquatic vehicle," *Drones*, vol. 8, no. 3, 2024, Art. no. 100, doi: 10.3390/drones8030100.

[23] Y. Bi, Y. Jin, C. Lyu, Z. Zeng, and L. Lian, "Nezha-Mini: Design and locomotion of a miniature low-cost hybrid aerial underwater vehicle," *IEEE Robot. Automat. Lett.*, vol. 7, no. 3, pp. 6669–6676, Jul. 2022, doi: 10.1109/LRA.2022.3176438.

[24] M. M. Maia, D. A. Mercado, and F. J. Diez, "Design and implementation of multirotor aerial-underwater vehicles with experimental results," in *Proc. IEEE/RSJ Int. Conf. Intell. Robots Syst.*, 2017, pp. 961–966.

[25] H. Alzu'bi, I. Mansour, and O. Rawashdeh, "Loon Copter: Implementation of a hybrid unmanned aquatic–aerial quadcopter with active buoyancy control," *J. Field Robot.*, vol. 35, no. 5, pp. 764–778, 2018, doi: 10.1002/rob.21777.

[26] Y. H. Tan and B. M. Chen, "Thruster allocation and mapping of aerial and aquatic modes for a morphable multimodal quadrotor," *IEEE/ASME Trans. Mechatron.*, vol. 25, no. 4, pp. 2065–2074, Aug. 2020, doi: 10.1109/TMECH.2020.2998329.

[27] X. Liu et al., "TJ-FlyingFish: Design and implementation of an aerial-aquatic quadrotor with tiltable propulsion units," in *Proc. IEEE Int. Conf. Robot. Automat.*, 2023, pp. 7324–7330, doi: 10.1109/ICRA48891.2023.10160899.

[28] L. Li et al., "An Aerial–Aquatic hitchhiking robot with remora-inspired tactile sensors and thrust vectoring units," *Adv. Intell. Syst.*, 2023, Art. no. 2300381, doi: 10.1002/aisy.202300381.

[29] K. Qin et al., "An aerial–Aquatic robot with tunable tilting motors capable of multimode motion," *Adv. Intell. Syst.*, vol. 5, no. 11, 2023, Art. no. 2300193, doi: 10.1002/aisy.202300193.

Yi Sun received the B.S. degree in mechanical electronics engineering from the Nantong University, Nantong, China, in 2021. He is currently working toward the Doctoral degree in mechanical engineering from the Nanjing University of Aeronautics and Astronautics, Nanjing, China.

His current research interests include aerial-aquatic robots, aerial-wall vehicles, and adaptive control.

Youzhi Xu received the B.S. degree in agricultural mechanization and automation from the Nanjing Agricultural University, Nanjing, China, in 2023. He is currently working toward the M.S. degree in mechanical engineering from the Nanjing University of Aeronautics and Astronautics, Nanjing, China.

His current research interests include extreme environment robot, cross-domain robot vehicles, and adaptive control.

Kaijie Lu (Student Member, IEEE) received the M.S. degree in aerospace science and engineering in 2024 from the Nanjing University of Aeronautics and Astronautics, Nanjing, China, where he is currently working toward the Doctoral degree in aerospace science and engineering.

His current research interests include flapping-wing micro air vehicle optimization design, and modeling.

Pengfei Li received the M.S. degree in aerospace science and technology engineering from the Nanjing University of Aeronautics and Astronautics, Nanjing, China, in 2024.

His research interests include micro aerial vehicles design and control, as well as UAV swarm collaborative planning.

Huan Shen received the B.S. degree from Central South University, Changsha, China, in 2016, and the Ph.D. degree from the Nanjing University of Aeronautics and Astronautics, Nanjing, China, in 2023, both in mechanical engineering.

He is currently an Assistant Researcher with the Nanjing University of Aeronautics and Astronautics. His research interests include micro robot design and robotics control.

Jiajun Xu (Member, IEEE) received the B.S. degree from the Hefei University of Technology, Hefei, China, in 2016, and the Ph.D. degree from the University of Science and Technology of China, Hefei, China, and the City University of Hong Kong, Hong Kong, in 2021, both in mechanical engineering.

He is currently an Assistant Professor with the College of Mechanical and Electrical Engineering. His research interests include rehabilitation robotics, biomimetic robotics, human–robot interaction control, and machine learning.

Yadong Gao received the Ph.D. degree in aeronautical engineering from the Nanjing University of Aeronautics and Astronautics, Nanjing, China, in 2004.

He is currently an Associate Professor and Specially-hired researcher with the College of Aerospace Engineering. He visited the University of Nottingham as a visiting scholar. He has authored or coauthored more than 60 academic papers in his research interests, which include helicopter design and its dynamics control, health, and usage monitoring of helicopter.

Dr. Gao was the recipient of the Second Prize for Teaching Achievements in Jiangsu Province, the Teaching Excellence Award of NUAA, and the Outstanding Class Teacher Award of NUAA.

Qijun Zhao received the Ph.D. degree in aerospace science and technology from the Nanjing University of Aeronautics and Astronautics, Nanjing, China, in 2005.

He is a Chairman of Helicopter Branch with the Chinese Society of Aeronautics and Astronautics. He is currently a Professor with the College of Aerospace. He visited the University of Maryland as a Research Fellow. He has authored or coauthored more than 350 papers in referred international journals and obtained more than 50 authorized inventions in his research interests, which include helicopter computational fluid dynamics and aerodynamics.

Aihong Ji (Member, IEEE) received the Ph.D. degree in mechanical engineering from the Nanjing University of Aeronautics and Astronautics, Nanjing, China, in 2007.

He visited Konkuk University and the University of Glasgow as a Research Fellow. He is currently a Professor with the College of Mechanical and Electrical Engineering. He has authored and coauthored more than 100 articles in refereed international journals and obtained more than 30 authorized inventions in his research interests, which include biomimetic robotics and intelligent equipment.

Dr. Ji was the recipient of one Gold Prize at the 39th Geneva International Invention Exhibition; one Second Prize of Natural Science Award from the Ministry of Education, China; one Second Prize of Technological Invention Award from the Ministry of Education, China.